



# Mesoporous silica supported Rh catalysts for high concentration N<sub>2</sub>O decomposition

Marco Piumetti <sup>a</sup>, Murid Hussain <sup>a,b</sup>, Debora Fino <sup>a</sup>, Nunzio Russo <sup>a,\*</sup>

<sup>a</sup> Department of Applied Science and Technology, Politecnico di Torino, Corso Duca degli Abruzzi 24, 10129 Torino, Italy

<sup>b</sup> Department of Chemical Engineering, COMSATS Institute of Information Technology, M.A. Jinnah Building, Defence Road, Off Raiwind Road, Lahore 54000, Pakistan

## ARTICLE INFO

### Article history:

Received 1 September 2014

Received in revised form

29 September 2014

Accepted 3 October 2014

Available online 12 October 2014

### Keywords:

N<sub>2</sub>O decomposition

Adipic acid plant

Rh catalyst

Mesoporous silica

MCF

## ABSTRACT

A set of Rh-containing catalysts (Rh-MCM-41, Rh-SBA-15, Rh-KIT-6 and Rh-MCF, nominal Rh content = 1 wt.%) has been prepared by wet impregnation of mesoporous silicas and tested for high concentration N<sub>2</sub>O abatement. The physico-chemical properties of the materials have been investigated by means of complementary techniques.

The best performances, in terms of N<sub>2</sub>O decomposition, have been achieved for the Rh-MCF catalyst, due to the better textural properties of the MCF silica. In fact, the MCF-type support exhibits three-dimensional mesoporosity with ultra-large cells (up to 40 nm), which allow a uniform distribution of small RhO<sub>x</sub> particles ( $\approx$ 1 nm) over the high (internal) surface area of the MCF. Moreover, the Rh active sites are also readily accessible to N<sub>2</sub>O molecules.

The most promising catalyst has shown the highest amount of Rh<sup>1+</sup> species, the easiest rhodium reducibility and the greatest abundance of Rh surface sites. These important features reflect the different Rh particle sizes and play a role in catalytic activity.

A remarkable relationship between the catalytic activity and the dimension of the RhO<sub>x</sub> particles has been observed in the 1–2.5 nm size domain, thus confirming the dispersion-sensitivity of N<sub>2</sub>O decomposition over RhO<sub>x</sub> nanoparticles.

© 2014 Elsevier B.V. All rights reserved.

## 1. Introduction

Nitrous oxide (N<sub>2</sub>O) is considered a greenhouse gas since it lasts approximately 150 years in the atmosphere, it has 310 and 21 times greater warming potential than CO<sub>2</sub> or CH<sub>4</sub>, respectively, and it contributes to the destruction of stratospheric ozone [1–3]. For these reasons, it has recently received a great deal of attention by scientists because of its possible environmental effects [1]. Europe has agreed to reduce greenhouse emissions, including N<sub>2</sub>O, to fulfil the Kyoto protocol.

N<sub>2</sub>O is produced from both natural and anthropogenic sources. Biological processes, which take place in soils and oceans, are the primary natural sources of N<sub>2</sub>O. The main contributors of the anthropogenic sources include fertilizers, nitric acid, adipic acid, caprolactam and glyoxal production, fossil fuels and biomass combustion, as well as sewage treatment [3,4]. Nitric acid and adipic acid production plants are thought to be the largest industrial

sources of N<sub>2</sub>O emissions. As a whole, there is a higher N<sub>2</sub>O concentration in tail gas emissions from adipic acid plants (usually 20–40% v/v) than from nitric acid production (around 300–3500 ppm). It has in fact been reported that around 10% of N<sub>2</sub>O released into the atmosphere each year originates from adipic acid production, and hence great efforts have been made to abate high-concentration N<sub>2</sub>O [5,6].

Catalytic N<sub>2</sub>O decomposition could be a promising alternative solution, as it makes N<sub>2</sub>O abatement possible at the emission source at lower temperatures (300–500 °C) than the conventional thermal abatement technology [3]. Noble metals, metal oxides, mixed oxides, metal or ion exchanged zeolites and supported metal catalysts have been reported in the literature as promising catalysts for N<sub>2</sub>O abatement [4–9]. Rhodium or iridium oxides have been found in particular to be more active in the decomposition of N<sub>2</sub>O than other oxides. However, their low surface areas contribute to their main disadvantages as catalysts [4,10]. Mesoporous materials with large controlled accessible surface areas could be attractive candidates for N<sub>2</sub>O decomposition, since the active phase can be highly dispersed over the support [11]. The discovery of ordered mesoporous molecular sieves, such as SBA-15

\* Corresponding author. Tel.: +39 011 0904710; fax: +39 011 0904699.

E-mail address: [nunzio.russo@polito.it](mailto:nunzio.russo@polito.it) (N. Russo).

and MCM-41, has sparked interest throughout the scientific community over the last few decades. These mesoporous silicas, first discovered by Mobil researchers, exhibit high surface areas and pore volumes with a highly ordered hexagonal array of large pores; thus, the diffusion of reactants to the catalytic sites is favoured compared to conventional zeolites. Owing to these interesting textural properties, ordered mesoporous materials have opened new and exciting opportunities in the field of heterogeneous catalysis [12–16].

Various types of noble metals supported on mesoporous silicas have recently been developed for low concentration N<sub>2</sub>O degradation and for nitric acid plant tail gas treatment application, and these have shown comparatively better activity than conventional catalysts due to the combination of good accessibility, uniform pore size and the high surface area of the mesoporous materials [4,15,17,18].

Rh supported on MCM-41, SBA-15-Conventional (SBA-15-C), Spherical shaped SBA-15 (SBA-15-S) and KIT-6 silica have been explored for the first time for low concentration N<sub>2</sub>O degradation in the recent works by the authors [4,18,19]. These Rh-based catalysts had shown good catalytic activity. However, to the best of the authors' knowledge, mesoporous silica supported noble metal (Rh) has not been explored yet for high concentration N<sub>2</sub>O abatement in the treatment of adipic acid production plant tail gas.

Therefore, in the current work, an effort has been made to explore mesoporous silica supported Rh catalysts for high concentration N<sub>2</sub>O abatement. Moreover, a recent mesoporous silica material, namely mesocellular silica foams (MCF), which features a well-defined three-dimensional (3D) mesoporosity with large pores (up to 40 nm) [20] has been investigated as a potential candidate for this application. Unlike MCM-41 or SBA-15, which have two-dimensional (2D) mesopore structures, MCF is a new three-dimensional (3D) hydrothermally robust material with ultra-large mesopores and uniform spherical cells interconnected by windows with a narrow size distribution [21–23]. This MCF-type material allows a good dispersion of the active phase (RhO<sub>x</sub> nanoparticles) and offers advantages, over its more ordered counterparts MCM-41 or SBA-15, in terms of better diffusion of reactants to the catalytic active sites.

MCM-41, SBA-15, KIT-6 and MCF have therefore been studied in the present work as supports for Rh-based catalysts (nominal Rh-content 1 wt.%) in order to obtain active catalysts for the abatement of high concentration N<sub>2</sub>O.

The structural and surface properties of the prepared catalysts have been investigated using complementary techniques, including X-ray diffraction (XRD), N<sub>2</sub> physisorption at -196 °C, field emission scanning electron microscope (FESEM), transmission electron microscope (TEM), H<sub>2</sub> temperature-programmed reduction (H<sub>2</sub>-TPR), X-ray photoelectron spectroscopy (XPS) and Fourier transform infrared spectroscopy (FT-IR) by adsorption of the basic probes (namely CO and NH<sub>3</sub>). Hence, the relationship between the physico-chemical properties and the catalytic performance of such materials has been studied.

## 2. Experimental

### 2.1. Preparation of the catalysts

Unless otherwise specified, all the ACS grade reagents were obtained from Sigma-Aldrich S.r.l. (Milan, Italy). The MCM-41 support was hydrothermally synthesized with a CTACl (cetyltrimethylammonium chloride surfactant), according to the procedure reported in Ref. [12]. The obtained MCM-41 material was then dried overnight at 100 °C, washed with distilled water and calcined at 550 °C for 5 h so that it could be used as a support.

The SBA-15 material was prepared by slightly modifying a literature procedure [24]. In a typical synthesis, 4 g of Pluronic P123 triblock copolymer (EO<sub>20</sub>PO<sub>70</sub>EO<sub>20</sub>,  $M_{av}$  = 5800) was dissolved in 30 g of bi-distilled water and 160 mL of 2 M HCl solution. Then, 8.5 g of TEOS (tetraethyl orthosilicate) was added and this solution was stirred at room temperature for 24 h. This was followed by ageing at 100 °C for another 24 h. Finally, the mixture was filtered, washed with distilled water, dried overnight at 100 °C and calcined at 550 °C for 5 h.

The KIT-6 support was prepared according to a procedure described elsewhere [25]. Briefly, 6 g of Pluronic P123 was dissolved in 217 g of distilled water and 11.8 g of concentrated HCl. Then, 6 g of 1-butanol (99.5%, Fluka) was added under stirring at 35 °C for 1 h. 12.9 g of TEOS was then added dropwise and the final solution was stirred at 35 °C for 24 h. The mixture was transferred to a Teflon autoclave and aged at 100 °C for 24 h. The solid was then recovered by filtration, washed with distilled water, dried overnight and calcined at 550 °C for 6 h.

The MCF support was synthesized by modifying a literature procedure [22], using Pluronic P123 surfactant with 1,3,5-trimethylbenzene (TMB) as the organic swelling agent with TMB/P123 = 0.75 (wt./wt.). In a typical synthesis, 4.0 g of Pluronic P123 and 3.0 g of 1,3,5-trimethylbenzene were dissolved in 150 mL of 1.6 M HCl solution and stirred at room temperature for 5 h. Then, 8.5 g of TEOS was added to the mixture and then stirred at 40 °C for 24 h. The milky reaction mixture was transferred to a Teflon autoclave and aged at 100 °C for another 24 h in order to increase both the cells and windows size of the foam. The solid product was filtered off, washed with distilled water and dried overnight at 100 °C under static conditions. The surfactant was removed by calcination at 600 °C for 5 h in air and the final mesoporous MCF material was obtained.

Calcined MCM-41, SBA-15, KIT-6 and MCF supported Rh (nominal Rh content = 1 wt.%) catalysts were synthesized by means of the incipient wetness method, using a rhodium nitrate precursor, followed by drying overnight at 100 °C and calcination at 600 °C for 6 h in air; the obtained catalysts were denoted as Rh-MCM-41, Rh-SBA-15, Rh-KIT-6 and Rh-MCF, respectively. A detailed description of the synthesis procedures and of the effect of the main operating parameters on the material properties can be found in Refs [12,22,24,25].

### 2.2. Characterization of the catalysts

Powder X-ray diffraction patterns have been collected on a Philips PW3040 diffractometer using Cu K $\alpha$  radiation ( $2\theta$  range = 0.5–60°; step = 0.02°·2 $\theta$ ; time per step = 1 s).

The textural properties of the prepared samples were obtained as follows: the BET (Brunauer–Emmett–Teller) specific surface area ( $S_{BET}$ ) was measured by means of N<sub>2</sub> sorption isotherms at -196 °C on a ca. 30 mg sample previously outgassed at 150 °C for 5 h to remove molecular water and other atmospheric contaminants (Micrometrics Tristar II, USA instrument); the total pore volume ( $V_p$ ) was calculated at  $p/p_0$  = 0.97, whereas the micropore volume ( $V_{micro}$ ) was measured according to the *t*-plot method; the average pore diameter ( $D_p$ ) was calculated by either applying the Barrett–Joyner–Halenda (BJH) algorithm to the isotherm desorption branch (MCM-41, SBA-15 and KIT-6 materials) or according to a modified Broekhoff de Boer (BdB) method using Hill's approximation for the adsorbed layer thickness (MCF materials) [26].

Sample morphology was investigated by means of an FESEM (Zeiss MERLIN, Gemini-II column) and TEM (Jeol JEM 3010 operating at 200 kV). The Rh-content was determined through EDS analysis (Oxford X-Act). Five different spots with a 10–50 nm diameter were selected in representative zones of the sample and the average Rh-content was then calculated.

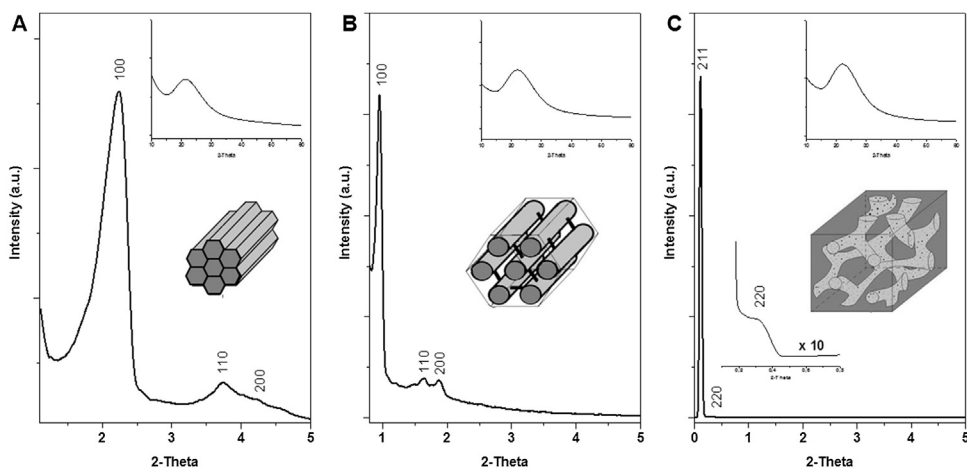


**Fig. 1.** Powder XRD patterns of the Rh-MCM-41 with (A), Rh-SBA-15 (B) and Rh-KIT-6 (C) samples and the respective representation of their pore topology.

H<sub>2</sub>-TPR analysis was carried out in a Thermoquest TPD/R/O 1100 analyzer equipped with a thermal conductivity (TCD) detector: a 50 mg sample was placed in a quartz tube, put in contact with reducing flowing gas (4.95% molar H<sub>2</sub> in Ar, 40 cm<sup>3</sup> min<sup>-1</sup>) and heated in the 25–850 °C temperature range (heating rate: 5 °C min<sup>-1</sup>), while H<sub>2</sub> consumption was recorded using a thermal conductivity detector (TCD).

XPS measurements were obtained on an XPS PHI 5000 Versa probe apparatus using a band-pass energy of 187.85 eV, 45° take off angle and a 100.0 μm diameter X-ray spot size. Curve-fits were performed by means of Multipack 9.0 software.

IR spectra were collected on an FT-IR spectrophotometer (Equinox 55, Bruker), equipped with an MCT (Mercury Cadmium Telluride) cryodetector. In order to perform the IR measurements, powder samples were pressed into thin self-supporting wafers (density c.a. 10 mg cm<sup>-2</sup>). Pretreatments were carried out using a standard vacuum frame in an IR cell equipped with KBr windows. In order to remove water and other atmospheric contaminants, the wafers were outgassed for 1 h at either 150 °C or at 500 °C before adsorption of CO at a nominal –196 °C and of NH<sub>3</sub> at room temperature. Because of the weakness of the interaction with CO, adsorption was studied at the nominal temperature of liquid N<sub>2</sub>, by dosing increasing amounts of CO (in the 1–1500 Pa equilibrium pressures range) onto samples previously outgassed inside a special IR cell, which allowed the simultaneous dosing of CO and the addition of liquid N<sub>2</sub>. Likewise, NH<sub>3</sub> was dosed at room temperature in the 1–1500 Pa equilibrium pressure range, after which the reversible fraction of the adsorbate was removed through prolonged evacuation. After each experiment, an evacuation step was performed to study reversibility of the interaction.

### 2.3. Catalytic activity tests

Catalytic activity tests were performed in a continuous reactor, that is a quartz U-tube with inner diameter = 4 mm, heated by an electric furnace; temperature was measured by means of a thermocouple placed approximately in the middle of the catalytic bed. The catalyst (0.1 g, 250–450 μm particle size) was pre-treated in He (flow rate = 100 cm<sup>3</sup> min<sup>-1</sup>) for 1 h at 150 °C to remove any species adsorbed on the catalyst surface.

The gas flow was then switched from He to the reactive mixture: 20% v/v N<sub>2</sub>O and 10% v/v O<sub>2</sub> diluted in He were fed to the reactor with a gas hourly space velocity (GHSV) of 17,000 h<sup>-1</sup>. The catalytic reaction was started when the reaction temperature was stable at 150 °C. The temperature was then raised by 5 °C min<sup>-1</sup> from 150 °C to 600 °C and maintained there for 2 h.

The outlet composition was monitored through an NO<sub>x</sub>/N<sub>2</sub>O NDIR (ABB) analyzer as a function of the bed temperature. The catalytic activity was evaluated, in terms of N<sub>2</sub>O conversion, C<sub>N<sub>2</sub>O</sub> (%), according to the following equation:

$$C_{N_2O}(\%) = \frac{C_{N_2O\text{ in}} - C_{N_2O\text{ out}}}{C_{N_2O\text{ in}}} \times 100$$

Each test was repeated three times to ensure reproducibility of the obtained results: the maximum deviation from the mean value over the three tests was ±5 °C. Temperatures corresponding to 10%, 50% and 90% N<sub>2</sub>O conversion (denoted as T<sub>10%</sub>, T<sub>50%</sub> and T<sub>90%</sub>, respectively) were taken as indices of the activity of the tested catalysts.

## 3. Results and discussion

### 3.1. Textural properties of the materials

Fig. 1 shows the XRD spectra of the Rh-MCM-41, Rh-SBA-15 and Rh-KIT-6 samples at low 2θ angles. Conversely, MCF-type materials do not exhibit any diffraction peaks in the 2θ = 0.5–5° region, as reported elsewhere [22,27]. As a whole, the XRD patterns of the ordered mesoporous materials are in agreement with the respective structures [28–31].

The XRD spectra of Rh-MCM-41 (Fig. 1A) show three peaks, due to the ordered hexagonal array of unidimensional silica channels, which can be indexed as (1 0 0), (1 1 0) and (2 0 0) planes [29]. MCM-41 exhibits long-range periodicity in two directions. The regular arrangement of the pores can be considered as a type of “superstructure” with long-range ordering.

The wide-angle XRD pattern of the same sample (the inset in Fig. 1A) shows a broad signal centred at 2θ = 23°, corresponding to amorphous silica, whereas no reflection peaks of Rh can be observed at high 2θ angles, thus indicating high Rh dispersion over the mesoporous support [18]. Similarly, the Rh-SBA-15 sample (Fig. 1B) only exhibits the diffraction peaks attributed to the (1 0 0), (1 1 0) and (2 0 0) reflections of the SBA-15 hexagonal space group p6mm [29].

The XRD spectra of the Rh-KIT-6 sample (Fig. 1C) displays two peaks at low 2θ angles, which can be assigned to the (2 1 1) and (2 2 0) planes of the 3-D cubic structure (*Ia3D* symmetry), whereas no Rh signal appears at higher 2θ angles (the inset in Fig. 1C) [31].

Table 1 shows the main textural properties of the catalysts, derived from both the EDS patterns and N<sub>2</sub> physisorption isotherms. As a whole, the prepared catalysts exhibit high surface areas (in the 590–902 m<sup>2</sup> g<sup>-1</sup> range) and total pore volumes

**Table 1**

Textural properties of the catalysts as obtained from both EDS analysis and N<sub>2</sub> sorption at –196 °C.

Catalyst	Rh-content <sup>a</sup> (wt.%)	S <sub>BET</sub> (m <sup>2</sup> g <sup>-1</sup> )	V <sub>p</sub> <sup>b</sup> (cm <sup>3</sup> g <sup>-1</sup> )	V <sub>micro</sub> <sup>c</sup> (cm <sup>3</sup> g <sup>-1</sup> )	D <sub>p</sub> (nm)	Rh-surface density (Rh nm <sup>-2</sup> )
Rh-MCM-41	1.2	902	0.69	0.00	3 <sup>d</sup>	0.08
Rh-SBA-15	1.4	650	0.63	0.04	5 <sup>d</sup>	0.13
Rh-KIT-6	1.4	687	0.96	0.02	6 <sup>d</sup>	0.12
Rh-MCF	0.9	596	1.51	0.02	25 <sup>e</sup> ; 14 <sup>f</sup>	0.09

<sup>a</sup> Measured by means of EDS analysis on 10–50 nm spots chosen in representative zones of the sample.

<sup>b</sup> Total pore volume.

<sup>c</sup> Micropore volume.

<sup>d</sup> Pore diameter calculated according to the BJH method from the N<sub>2</sub> isotherm desorption branch.

<sup>e</sup> Cell diameter determined from adsorption branches of the N<sub>2</sub> isotherms (BdB-FHH method).

<sup>f</sup> Window diameter determined from the desorption branches of the N<sub>2</sub> isotherms (BdB-FHH method).

(0.63–1.51 cm<sup>3</sup> g<sup>-1</sup>), which allow a good dispersion of the active phase. Moreover, both the KIT-6 and MCF-type materials (the latter can be seen in Scheme 1) have the advantage of having 3-D mesoporous structures, which should render the Rh dispersion easier.

Table 1 reports the Rh-surface densities (number of Rh atoms per nm<sup>2</sup>) calculated considering: (i) the Rh content determined through the EDS analysis and (ii) the S<sub>BET</sub> on the samples studied. The obtained values confirm that high Rh dispersion has been achieved for the catalysts (in the 0.08 to 0.14 Rh nm<sup>-2</sup> range). These findings suggest that RhO<sub>x</sub> nanoparticles should be distributed in a spatially isolated and uniform manner over the surface of the mesoporous solids.

Fig. 2 reports N<sub>2</sub> physisorption isotherms of the prepared catalysts, which exhibit type IV isotherms typical of mesostructured materials [32].

The Rh-MCM-41 isotherm (curve a) shows two distinct features: a sharp capillary condensation step at a relative pressure ( $p/p_0$ ) of about 0.3, and small hysteresis between the adsorption and desorption branches. The adsorption at very low  $p/p_0$  is due to monolayer adsorption of N<sub>2</sub> on the walls of the mesopores and does not reflect the presence of microporosity [30]; the small hysteresis loops seem to depend on the small-pore size of MCM-41 ( $\approx$ 3–4 nm), although there is still no unambiguous explanation of this phenomena [30]. Rh-SBA-15 (curve b) exhibits type IV isotherms with H1 hysteresis loops, which are characteristic of the SBA-15-type material [31,33]; the sharp increase in the 0.5–0.6  $p/p_0$  range is in fact due to capillary condensation within the mesoporous channels. Moreover, the shift towards higher  $p/p_0$  of the step corresponding to N<sub>2</sub> condensation in primary mesopores ( $p/p_0 \approx 0.6$ ) is consistent with the presence of larger pores ( $\approx$ 5 nm in diameter) [32,34]. The isotherms of Rh-KIT-6 (curve c) present a sharp capillary condensation step at slightly

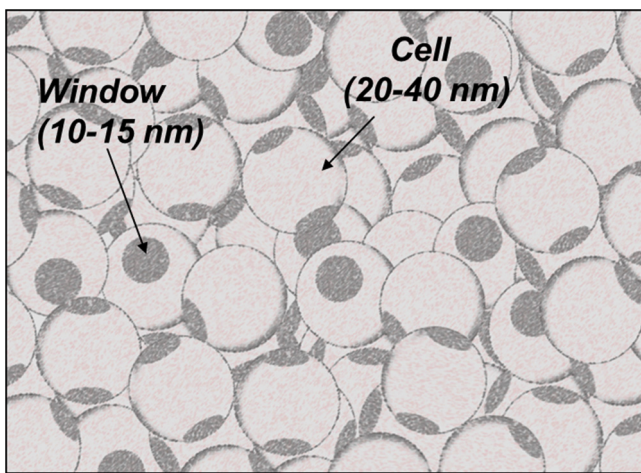
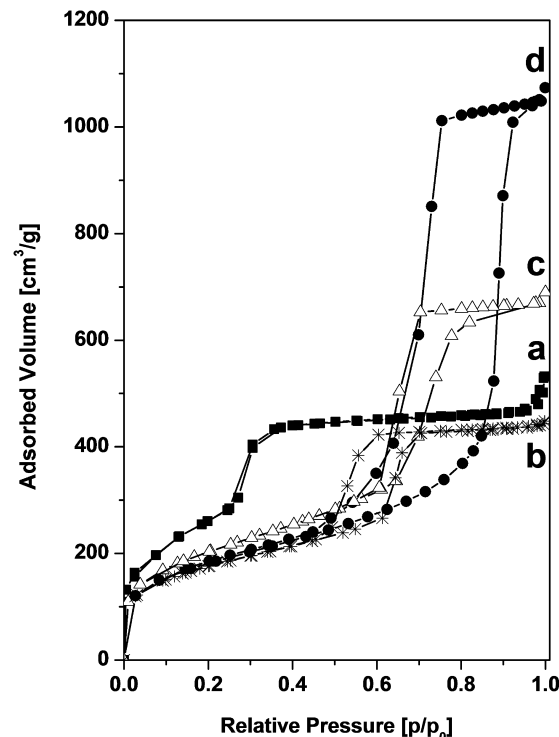
higher relative pressures (0.6–0.7  $p/p_0$ ), and a hysteresis loop that is characteristic of materials with a narrow pore size distribution (average pore diameter  $\approx$ 6–7 nm) [31].

Interestingly, the Rh-MCF sample (curve d) exhibits type IV isotherms, with H1 hysteresis loops shifted to a higher relative pressure (0.60–0.90  $p/p_0$ ), thus indicating the presence of ultra-large pores, namely “closed cells” ( $\approx$ 25 nm in diameter) interconnected to each other by small windows ( $\approx$ 14 nm) [29].

Fig. 3 reports the FE-SEM images of the prepared Rh-containing catalysts, in which the different morphologies of the materials are shown. As a whole, after Rh incorporation, there is no significant change in the shapes of the parent silica materials (not reported for the sake of brevity). The Rh-MCM-41 catalyst (Fig. 3a) reveals a hexagonal self-assembled structure, whereas the typical worm-like array of SBA-15 can be seen for the Rh-SBA-15 (Fig. 3b).

The morphology of the Rh-KIT-6 sample is shown in Fig. 3c, and is in agreement with those found in the literature. Moreover, the Rh-MCF catalyst (Fig. 3d) exhibits a spongy-like structure, which is typical of MCF-type materials.

The TEM images of the prepared materials are shown in Fig. 4. The microographies indicate that the RhO<sub>x</sub> particles have been



**Scheme 1.** Structure of the MCF-type material.

Fig. 2. N<sub>2</sub> physisorption isotherms measured at –196 °C on samples previously outgassed at 150 °C: Rh-MCM-41 (a), Rh-SBA-15 (b), Rh-KIT-6 (c) and Rh-MCF (d).

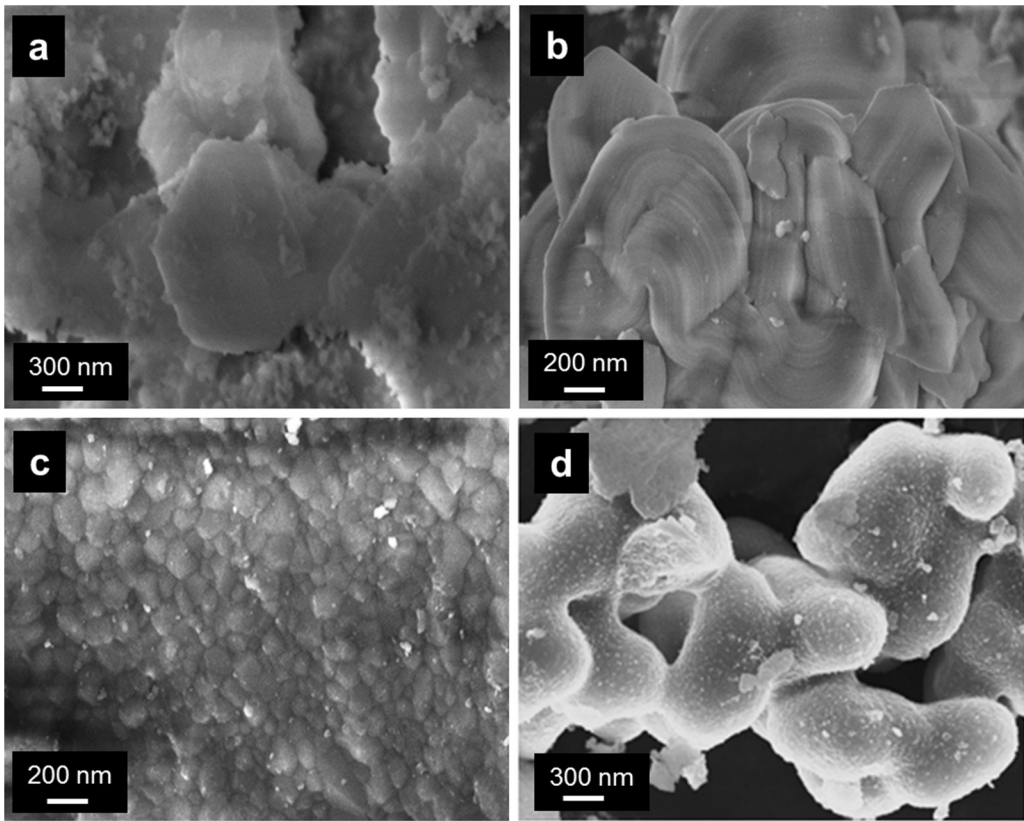


**Fig. 3.** FE-SEM images of the Rh-MCM-41 (a), Rh-SBA-15 (b), Rh-KIT-6 (c) and Rh-MCF (d) samples.

dispersed uniformly on the mesoporous silicas and no agglomerates have been found. However, different Rh particle sizes can be observed, due to the different textural characteristics of the support materials and will be discussed and correlated to the catalytic activity in the next section.

Well-ordered arrays of the 2-D mesoporous channels can be observed for both Rh-MCM-41 and Rh-SBA-15 samples (Fig. 4a and b, respectively), in agreement with their hexagonal arrangement of the uniform pores [11,35,36]. As is known, the SBA-15-type material channels are interconnected through micropores and this can be confirmed by the slightly higher micropore volume observed for the Rh-SBA-15 sample (Table 1). On the other hand, the Rh-KIT-6 sample (Fig. 4c) shows a 3-D mesoporous network in which the uniform channels ( $\approx$ 6–8 nm in size) are connected to each other [37]. Similarly, the TEM micrograph of the Rh-MCF sample (Fig. 4d) reveals a disordered array of 3-D mesoporous spherical cavities ( $\approx$ 25–30 nm in diameter), which is typical of the MCF-type material [27,38]. The measured cell sizes are in fair agreement with pore sizes determined from  $N_2$  isotherms (Table 1). Moreover, the wall thickness, which has also been estimated from the TEM pictures, is around 5–8 nm, and this result confirms the presence of rather thick and robust framework walls, as reported elsewhere [38].

TEM images of the  $RhO_x$  particles reveal mainly “hexagonal” structures (Fig. 4e), in agreement with the literature [39], although convex polyhedra structures faceted with planes can be also observed, as schematically shown in Fig. 4f. The equilibrium shape of a metal nanoparticle is in fact determined by the Wulff rule, according to which the convex envelope of planes minimizes the surface energy for a given enclosed volume.

The element distribution from EDS mapping also confirms that small  $RhO_x$  particles are well-dispersed (spatially isolated) on the surface of the MCF support (Fig. 5), as a consequence of its remarkable textural properties.

### 3.2. Nature and reducibility of the Rh species, as studied by means of XPS and $H_2$ -TPR measurements

Fig. 6 shows the Rh 3d XPS spectra of the catalysts in the 304.0–320.0 eV range. The binding energies at the 304.0–311.9 eV and 312.0–320.0 eV regions can be attributed to Rh 3d<sub>5/2</sub> and Rh 3d<sub>3/2</sub>, respectively [40–42]. The Rh 3d<sub>5/2</sub> BE region has been reported to occur at 307.9 eV, or lower, for  $Rh^0$ , in the 308.0–308.9 eV range for  $Rh^{+1}$  and at 309.0, or higher, for  $Rh^{3+}$  [4,40–44]. The relative abundance of the surface  $Rh^0$ ,  $Rh^{+1}$  and  $Rh^{3+}$  species of each sample has been calculated by considering the deconvolution of the Rh 3d<sub>5/2</sub> signal (Table 2). As a whole, the results have pointed out that the  $RhO_x$  nanoparticles supported over the mesoporous silicas exhibit much more  $Rh^{+1}$  than  $Rh^{3+}$  or  $Rh^0$  species. According to the literature, the catalytic activity of Rh-based catalysts towards  $N_2O$  decomposition is favoured by the presence of Rh species in a non-stoichiometric state, which is between Rh and  $Rh_2O_3$  [41]. The highest amount of  $Rh^{+1}$  species has been observed for the Rh-MCF sample (namely 90.1 at.%); the latter sample has also shown the lowest  $Rh^{3+}/Rh^{+1}$  ratio, whereas the presence of metallic Rh is negligible (0.1 at.%). These findings reflect the small sizes of the  $RhO_x$  particles (mean diameter = 1.0 nm) that are finely dispersed over the MCF-type support: the surface Rh species become oxidized to  $Rh^+$  by  $O_2$  or  $-OH$  groups, which are present at the metal-support interface [39]. Higher amounts of the surface  $Rh^0$  and  $Rh^{3+}$  species appear at the surface of the other catalysts, and the  $Rh^{3+}/Rh^{+1}$  ratios follow the Rh-KIT-6 < Rh-SBA-15 < Rh-MCM-41 order. These XPS data seem to be correlated to the particle size (values shown in Table 3): the smaller the Rh particle, the higher the surface  $Rh^+$  species.

The reducibility of the surface and bulk Rh species has been investigated through  $H_2$ -TPR analysis. Fig. 7 shows the  $H_2$ -TPR profiles of the fresh samples. As a whole, a low-temperature reduction

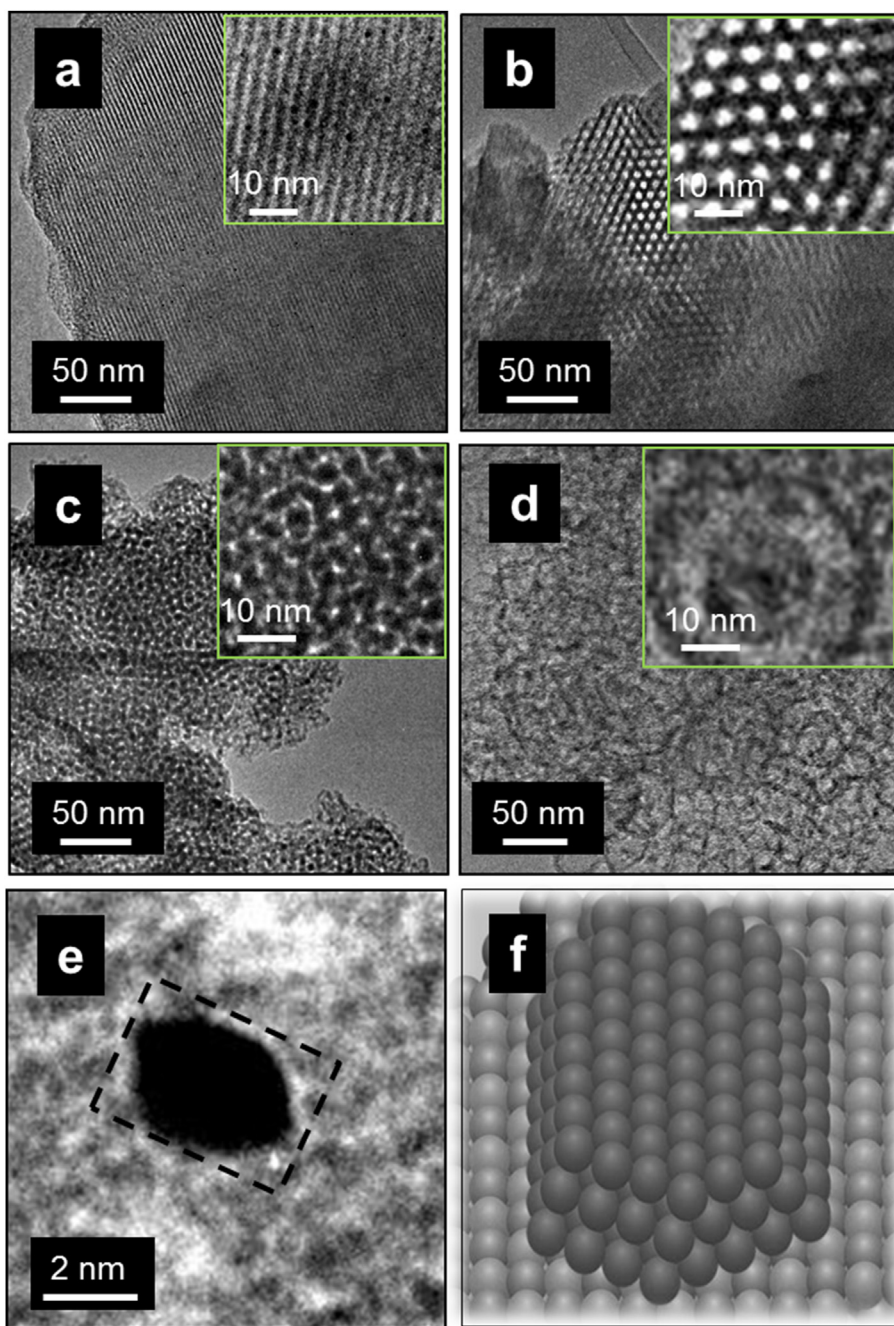


**Fig. 4.** TEM images of the Rh-MCM-41 (a), Rh-SBA-15 (b), Rh-KIT-6 (c) and Rh-MCF (d) samples. TEM image of a single hexagonal  $\text{RhO}_x$  nanoparticle supported on MCF (e) and schematic representation of a  $\text{RhO}_x$  nanoparticle (f).

peak appears in the 120–153 °C range, which can be attributed to the surface  $\text{RhO}_x$  reduction, while multiple peaks appear at higher temperatures (335–450 °C), due to bulk reduction [45,46]. However, the TPR profiles of these Rh-based catalysts depend to a great

extent on the location (chemical environment) and dimension of the  $\text{RhO}_x$  particles [45–47]. An easier surface Rh reduction has been obtained for both the Rh-MCF and Rh-KIT-6 samples (reduction peaks at 120 and 124 °C, respectively), compared to Rh-SBA-15 and

**Table 2**

Results of curve-fittings on the Rh 3d<sub>5/2</sub> peaks in the XP spectra of the catalysts: the maximum position (eV) is reported along with the corresponding atomic percentage for the Rh<sup>3+</sup>, Rh<sup>1+</sup> and Rh<sup>0</sup> species.

Sample	Rh <sup>3+</sup> (% atom)	Rh <sup>3+</sup> BE (eV)	Rh <sup>1+</sup> (% atom)	Rh <sup>1+</sup> BE (eV)	Rh <sup>0</sup> (% atom)	Rh <sup>0</sup> BE (eV)	$\frac{\text{Rh}^{3+}}{\text{Rh}^{1+}}$
Rh-MCM-41	34.9	309.9	56.0	308.9	9.1	306.5	0.62
Rh-SBA-15	22.8	310.0	60.5	308.1	16.7	306.5	0.38
Rh-KIT-6	21.3	309.3	64.5	308.9	14.2	306.9	0.33
Rh-MCF	9.8	310.2	90.1	308.9	0.1	307.8	0.11

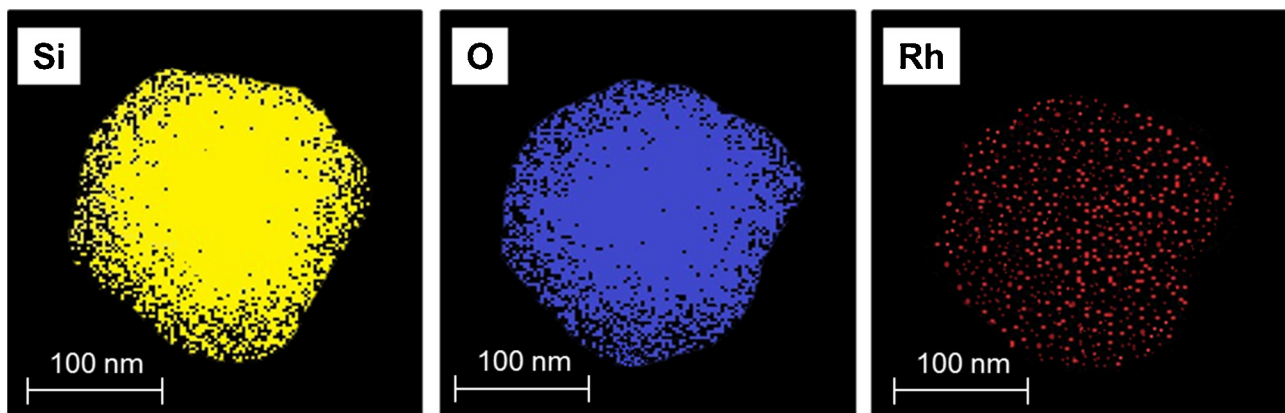


**Fig. 5.** EDS mapping of the Rh-MCF catalyst.

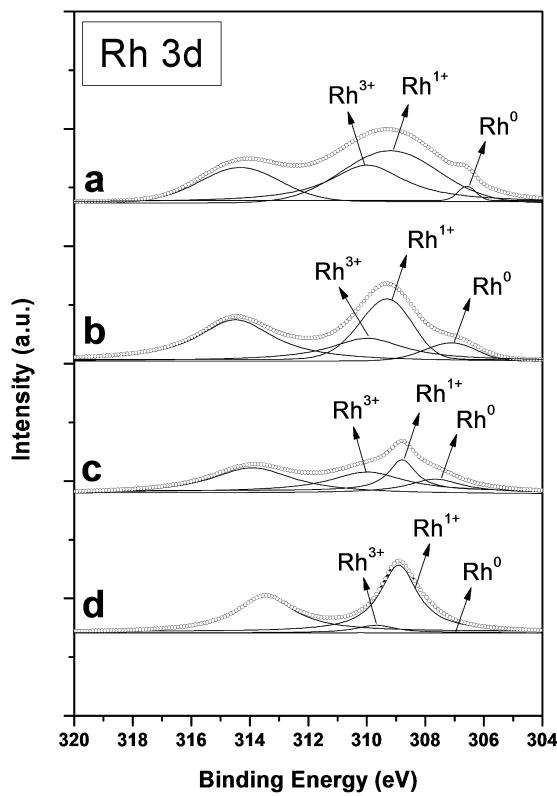


**Fig. 6.** XPS spectra of the (a) Rh-MCM-41, (b) Rh-SBA-15, (c) Rh-KIT-6 and (d) Rh-MCF samples in the Rh (3d) core level regions.

Rh-MCM-41 (peaks at 152–153 °C). These findings reflect the different Rh particle sizes: small RhO<sub>x</sub> particles can be reduced more easily than larger ones [42].

Moreover, the relative abundance of the Rh surface sites calculated for the Rh-MCF catalyst ( $\approx 36\%$  of the total number of Rh active sites) through the deconvolution analysis of the H<sub>2</sub>-TPR

**Table 3**

Mean size of the RhO<sub>x</sub> particles for the prepared catalysts.

Sample	Rh particle size <sup>a</sup> (nm)	N
Rh-MCM-41	2.3 ± 0.3	118
Rh-SBA-15	1.9 ± 0.3	50
Rh-KIT-6	1.2 ± 0.4	66
Rh-MCF	1.0 ± 0.4	53

<sup>a</sup> Mean Rh particle sizes measured by  $\sum d_i/N$ , where N is the total number of particles considered in the TEM images and  $d_i$  is the summation index.

profiles, appears much higher than those observed for the other catalysts (in the 17–21% range). Hence, the surface area and total volume of Rh particle ratio is much larger for the Rh-MCF catalyst. In agreement with the literature, the small metal particles are more reactive than the larger ones, since the electronic state and defect density change markedly at a critical size of about 2 nm [48]. A decrease in particle size increases the number of surface atoms with low-coordination numbers, such as corners and edges, which in turn tends to increase the reactivity normalized to exposed atoms. Moreover, due to the considerably higher atomic flexibility of the lattice of the small metal particles, compared to larger structures, the interior of the nanoparticles may actively participate in reactions, and have a decisive influence on the adsorption and catalytic properties [49,50].

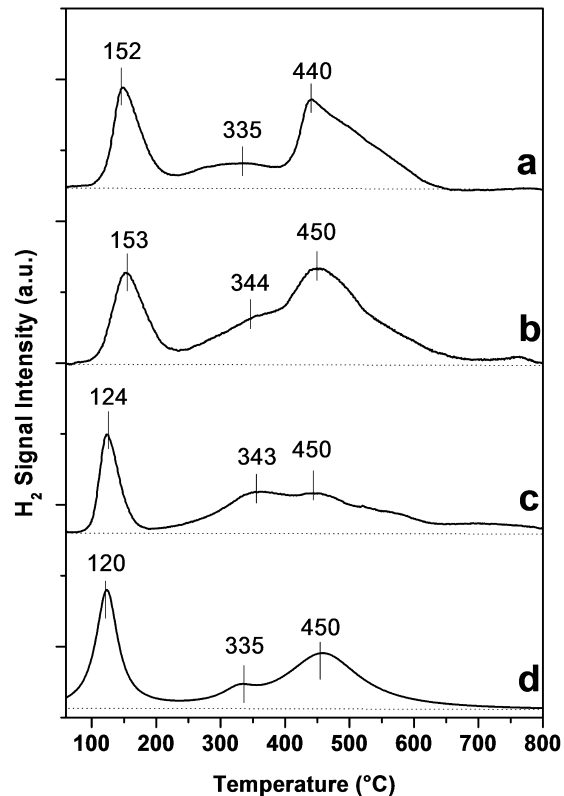


**Fig. 7.** H<sub>2</sub>-TPR profiles of the (a) Rh-MCM-41, (b) Rh-SBA-15, (c) Rh-KIT-6 and (d) Rh-MCF samples.

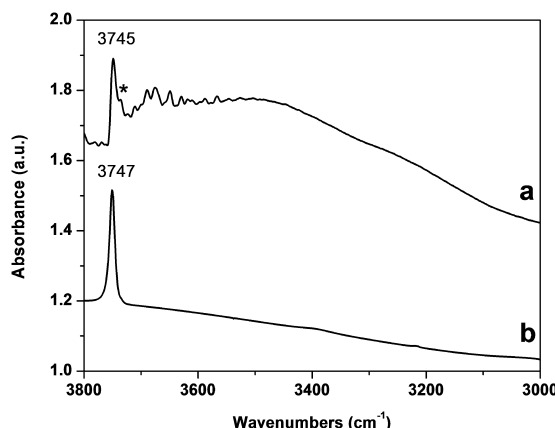


**Fig. 8.** FT-IR spectra, in the 3800–3000 cm<sup>-1</sup> range, of the Rh-MCF outgassed at 150 (curve a) and 500 °C (curve b).

### 3.3. FT-IR study of surface acidic properties

The acidity of the surface hydroxyl groups and of the Rh active sites has been investigated by means of NH<sub>3</sub> and CO adsorption on the Rh-MCF catalyst.

Fig. 8 reports the FT-IR spectra in the OH stretch region (3800–3000 cm<sup>-1</sup>) of the Rh-MCF sample outgassed at 150 and 500 °C, before the adsorption experiments. The spectra exhibit a sharp band at 3747–3745 cm<sup>-1</sup>, assigned to isolated silanols, which is usually seen at the surface of mesoporous silicas [22,34]. On the sample outgassed at 150 °C (curve a), the bands corresponding to the H-bonded silanols appear as a weak signal at about 3730 cm<sup>-1</sup> (asterisk) and as a broad absorption below 3700 cm<sup>-1</sup>. The former can be assigned to the terminal silanols of H-bonded SiOH chains, whereas the H-bonded silanols inside the chains absorb below 3700 cm<sup>-1</sup> [22]. After outgassing at 500 °C (curve b), only the band of isolated silanols can be observed in the spectra, thus showing that H-bonded hydroxyls were removed at a high temperature through surface dehydration, with the formation of isolated SiOH.

Fig. 9 shows the difference spectra recorded after dosing NH<sub>3</sub> on the Rh-MCF sample outgassed at 150 and 500 °C, obtained after subtracting the bare spectra. After ammonia adsorption on the sample outgassed at 150 °C (Fig. 9A), a band grew at ca. 1465 cm<sup>-1</sup>, and shifted slightly with coverage towards higher wavenumbers, which were assigned to the bending vibration of the ammonium species that formed on the Brønsted hydroxyls [34]. Correspondingly, in the OH stretching region, three bands decreased at 3745, 3690 and 3555 cm<sup>-1</sup> due to different kinds of hydroxyls interacting with NH<sub>3</sub>. The first band is due to free silanols, whereas those at 3690 and 3555 cm<sup>-1</sup> are related to the terminal and H-bonded silanols in the hydroxyls chains, respectively [51]. At lower wavenumbers, a band can be seen at 1627 cm<sup>-1</sup>, due to NH<sub>3</sub> molecules H-bonded to silanols. Evacuation at room temperature does not lead to the complete removal of adsorbed ammonia: weak signals, due to the NH<sub>3</sub> molecules still interacting with the surface, can be observed in the corresponding spectrum (bold curve). After ammonia dosage on the sample outgassed at 500 °C (Fig. 9B), the band due to isolated silanols decreased in the OH stretching range, in agreement with the fact that more acidic hydroxyls were removed by dehydration (vide supra). The corresponding bending mode of NH<sub>3</sub> interacting with silanols via H-bond can be observed at 1635 cm<sup>-1</sup>. Residual H-bonded silanols give rise to the formation of ammonium ions (bending mode at 1467 cm<sup>-1</sup>), whereas more acidic hydroxyl groups (i.e. the majority of H-bonded silanols) are removed at 500 °C. An additional band can be seen at low wavenumbers (1612 cm<sup>-1</sup>), due to NH<sub>3</sub> adducts with Rh ions (acting as Lewis acidic centres). These are well-exposed at the surface

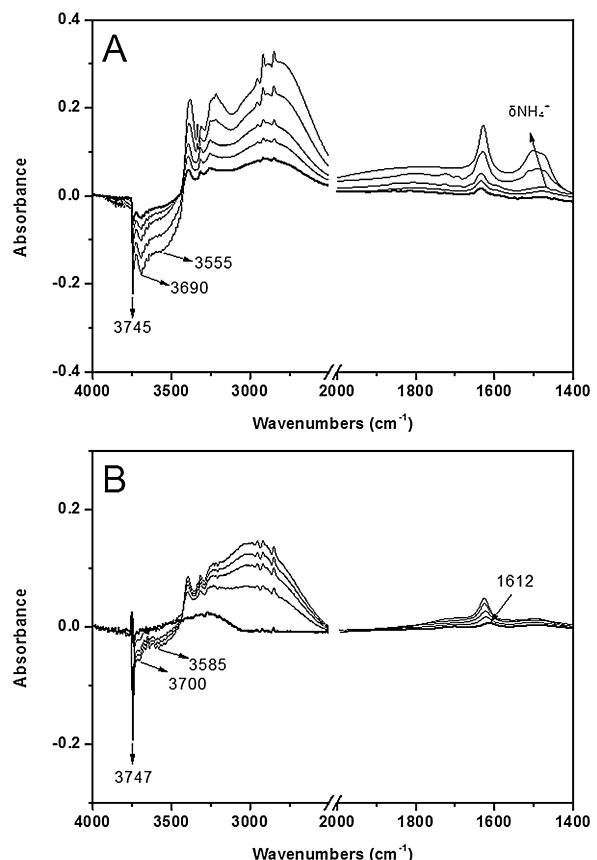


**Fig. 9.** FT-IR difference spectra recorded after dosing NH<sub>3</sub> at room temperature on Rh-MCF outgassed at 150 (Section A) and 500 °C (Section B). Partial NH<sub>3</sub> pressures in the 1–1500 Pa range. Bold curves: spectra taken after 30 min evacuation at room temperature to verify adsorption reversibility.

after de-hydroxylation [52]. As reported in the literature, interaction of N<sub>2</sub>O molecules with the active catalyst centres takes place via a charge donation from the catalyst (Rh active sites) to the antibonding orbitals of N<sub>2</sub>O [39].

CO adsorption has been studied at the temperature of liquid N<sub>2</sub> to better evaluate the nature of surface hydroxyls. Fig. 10 shows the difference spectra attained after dosing CO (1–1500 Pa equilibrium pressure range) on the Rh-MCF sample outgassed at 150 °C (Section A) and 500 °C (Section B). Negative and positive bands correspond to species either disappearing or forming upon interaction with CO, respectively. After CO dosage on the sample outgassed at 150 °C, two negative bands can be observed in the OH stretching region (3800–3000 cm<sup>-1</sup>) at 3745, 3715 and 3705 cm<sup>-1</sup>. These have been assigned to different kind of hydroxyls interacting with the CO molecules through H bonding: (i) isolated silanols (3745 cm<sup>-1</sup>), (ii) terminal H-bonded silanols (3715 cm<sup>-1</sup>) and (iii) –OH groups of silica strongly polarized by interaction with the vicinal Rh atoms (3705 cm<sup>-1</sup>) [22,51,53].

The more acidic the hydroxyls, the greater the observed shift: (i) species absorbing at 3705 cm<sup>-1</sup> shifted to 3450 cm<sup>-1</sup> ( $\Delta\nu=255$  cm<sup>-1</sup>); (ii) the H-bonded silanol band at 3715 cm<sup>-1</sup> shifted to 3590 cm<sup>-1</sup> ( $\Delta\nu=125$  cm<sup>-1</sup>); (iii) the free silanols band at 3745 cm<sup>-1</sup> shifted to 3648 cm<sup>-1</sup> ( $\Delta\nu=98$  cm<sup>-1</sup>). In the CO stretching region (inset in Fig. 10A), two bands form at 2156 and 2137 cm<sup>-1</sup>, respectively assigned to (i) CO molecules H-bonded to hydroxyls and (ii) a liquid-like phase [22,51]. The weak signal at 2110 cm<sup>-1</sup> can be ascribed to dicarbonyls formed as binuclear Rh<sup>+</sup> (CO)<sub>2</sub>···Rh<sup>+</sup>(CO)<sub>2</sub> complexes. The latter band confirms the presence of small Rh clusters finely dispersed over the surface of the

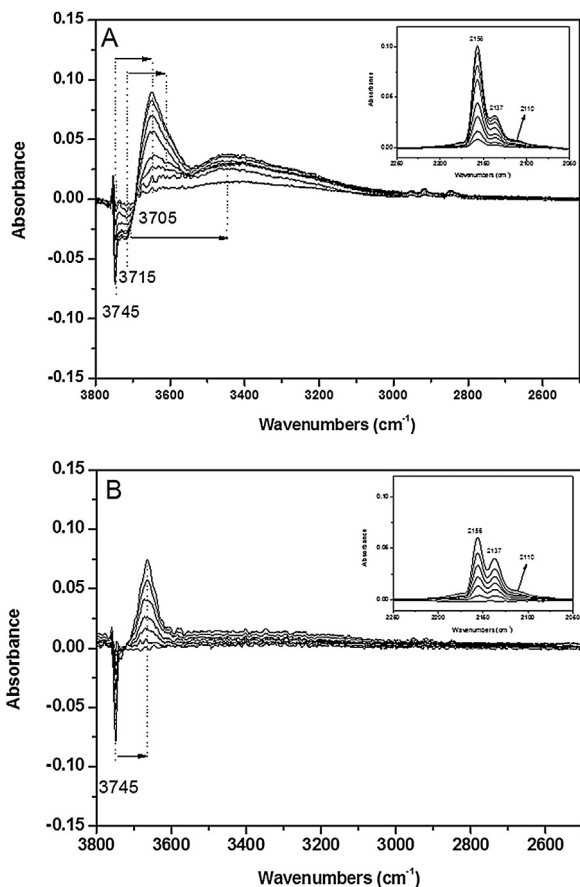


**Fig. 10.** FT-IR difference spectra, in the 3800–3000 cm<sup>-1</sup> region, recorded after dosing CO (equilibrium pressure in the 1–1500 Pa range) at nominal –196 °C on Rh-MCF outgassed at 150 °C (Section A) and 500 °C (Section B). Insets: same difference spectra, in the CO stretching region (2250–2050 cm<sup>-1</sup>).

nанопористый твердый [53–55]; кроме того, поверхность Rh атомы имеют формальную окислительную степень +1, что приводит к электронной конфигурации 4d<sup>8</sup>. [56].

CO, адсорбированный над Rh<sup>n+</sup> ионами ( $n > 1$ ) должен дать сигнал в диапазоне 2150–2120 cm<sup>-1</sup> [53,57], но соответствующий сигнал вероятно суперимпонирован на сигнал физисорбированного CO (2137 cm<sup>-1</sup>).

Когда Rh-MCF образец был выгнан при 500 °C (Fig. 10B), только характеристики изолированных силенолов (3745 cm<sup>-1</sup>,  $\Delta\nu = 90$  cm<sup>-1</sup>) остались, что указывает на предпочтительное удаление более кислых гидроксилов. Аналогично, в CO-располагающейся области (вставка), значительно менее интенсивный сигнал CO, адсорбированного на гидроксилах, появляется при 2156 cm<sup>-1</sup>. С другой стороны, большее количество Rh-поверхностных сайтов (действие как Льюис кислоты) можно увидеть при 2110 cm<sup>-1</sup>, как следствие поверхности дехидроксилирования, в соответствии с результатами, полученными из NH<sub>3</sub> адсорбции (виде спрота). Согласно литературе, поверхность Rh<sup>+</sup> частицы демонстрирует высокую Льюис кислотную реактивность и это может объяснить обещающуюся реактивность малых RhO<sub>x</sub> частиц в разложении N<sub>2</sub>O [6,58,59].

#### 3.4. Catalytic activity tests

Катализическое поведение в отношении разложения N<sub>2</sub>O было проверено в температурном диапазоне 150–600 °C. Fig. 11 показывает конверсию N<sub>2</sub>O как функция температуры, достигнутой с использованием Rh-содержащих катализаторов и MCF-силикатов. Как ожидается, N<sub>2</sub>O показывает незначительную конверсию в отсутствии активного фазы над температурным диапазоном (т.е. 7% конверсия N<sub>2</sub>O была получена для MCF-силиката при 600 °C), в то время как Rh-содержащие катализаторы показали положительные тенденции конверсии N<sub>2</sub>O для возрастающей температуры

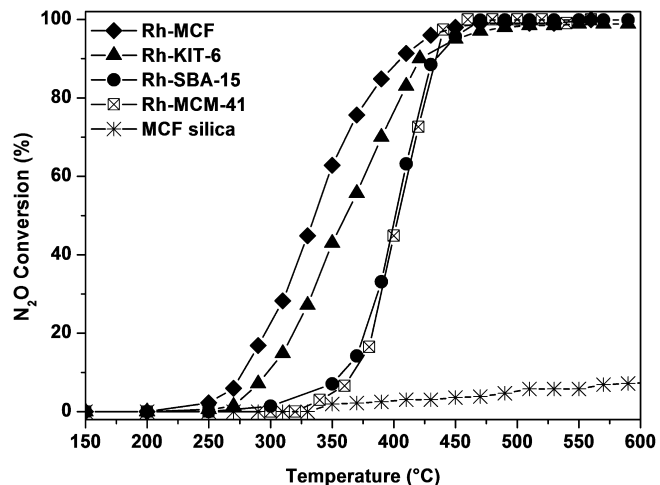


**Fig. 11.** N<sub>2</sub>O conversion as a function of temperature, over Rh-based catalysts and MCF silica.

температура. В целом, различные катализативные активности были обнаружены для катализаторов, и лучшие результаты, в терминах  $T_{10\%}$ ,  $T_{50\%}$  и  $T_{90\%}$  значений (температуры, необходимые для достижения 10%, 50% и 90% конверсии N<sub>2</sub>O, соответственно), были достигнуты для Rh-MCF катализатора (значения в Таблице 4).

The MCF-type material has 3-D mesoporosity with ultra-large cavities, which allows a uniform distribution of small RhO<sub>x</sub> particles over the high (internal) surface area. Moreover, the active sites are also readily accessible to reactants, as a consequence of their uniform distribution over the 3-D internal surface of MCF [22,23,45]. Similarly, the activity of the Rh-KIT-6 catalyst is lower than that of Rh-MCF, but higher than those of the Rh-SBA-15 and Rh-MCM-41 catalysts, thus reflecting the important role of the 3-D porous structure in favouring the active site dispersion.

The Rh-MCF catalyst appears closer to the concept of single-site heterogeneous catalysts (SSHС) proposed by Thomas [60,61]. In fact, the active sites (atoms of ensemble of atoms) are spatially well separated and uniformly distributed on solid surfaces. However, the structural complexity of small RhO<sub>x</sub> particles is much higher than that of true SSHCs, since the surface sites are not identical in chemical composition or in their atomic environment [62]. In fact, the surface properties can be altered by changing the size and shape of the nanoparticles, and hence various complexity structures of active sites may occur on the solid surface [63,64].

Fig. 12 shows the N<sub>2</sub>O conversion rates, normalized per mmol of Rh, as a function of the mean Rh particle sizes. A remarkable dependence of the catalytic rate on the dimension of the particles can be observed in the 1–2.5 nm size domain, thus showing the size-sensitivity [65–67] of N<sub>2</sub>O decomposition over RhO<sub>x</sub> particles.

This size-dependence can be ascribed either to the fact that low coordination surface sites exhibit higher reactivity, because of the low energy charge fluctuations in their d-bands or to the quantum size effects that are produced when electrons are confined within a small volume [68].

Fig. 13 shows the relationship between the mean Rh particle sizes of the prepared catalysts and their catalytic activities,

**Table 4**  
N<sub>2</sub>O decomposition activity results of the prepared supported Rh catalysts.

Catalyst	$T_{10\%}$ (°C)	$T_{50\%}$ (°C)	$T_{90\%}$ (°C)
Rh-MCM-41	366	405	435
Rh-SBA-15	357	403	430
Rh-KIT-6	297	360	421
Rh-MCF	277	335	407

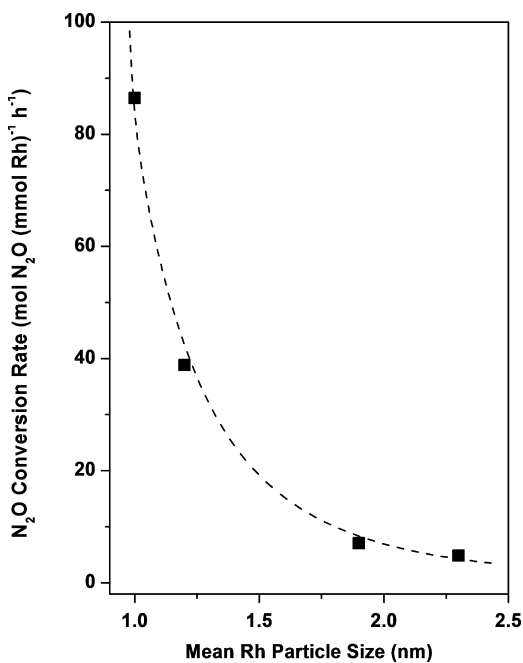


**Fig. 12.** N<sub>2</sub>O conversion rate at 350 °C, normalized per mmol of Rh, as a function of the RhO<sub>x</sub> particle size.

expressed in terms of temperature (°C), at which 10%, 50% and 90% N<sub>2</sub>O conversion is obtained ( $T_{10}$ ,  $T_{50}$  and  $T_{90}$ , respectively). As expected, better performances have been achieved for the smaller RhO<sub>x</sub> particles finely dispersed on the MCF-type material.

As is known, catalytic stability is an important feature for catalysts in industrial applications. Therefore, several tests have been carried out to consider the surface stability of the best performing catalyst. Inward relaxation and the reconstruction of the metal particles are much more marked at low coordination sites (i.e. steps and corners), which are more “flexible” and self-repair at higher

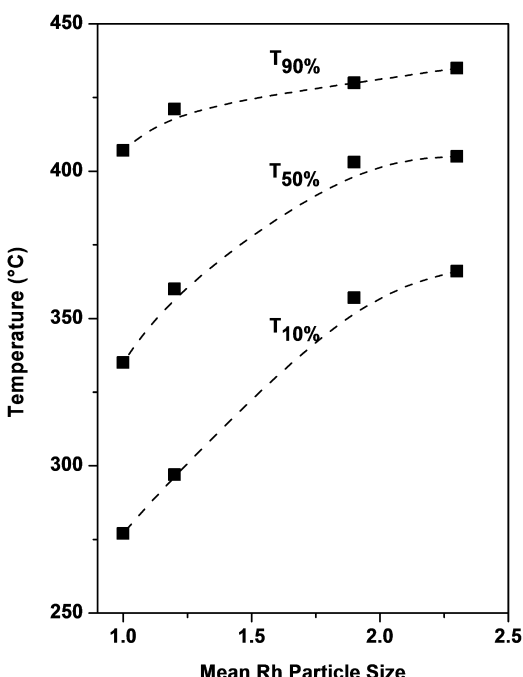


**Fig. 13.** Correlation between the temperature (°C) at which 10%, 50% and 90% N<sub>2</sub>O conversions are obtained ( $T_{10}$ ,  $T_{50}$  and  $T_{90}$ , respectively) as a function of the RhO<sub>x</sub> particle size.

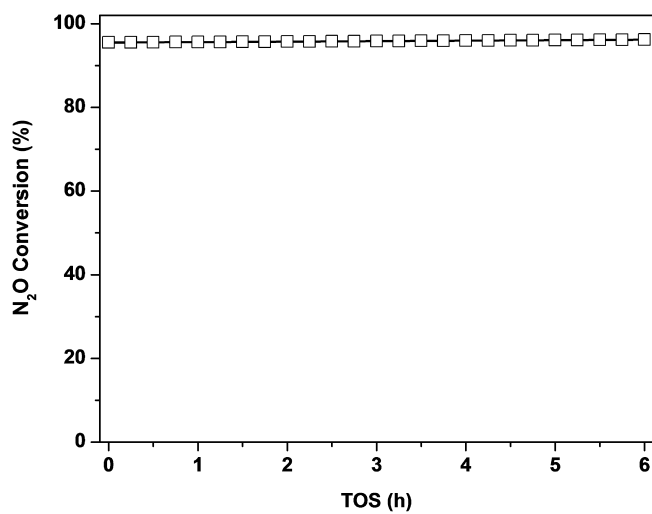


**Fig. 14.** Effect of time-on stream on the catalytic performance of the Rh-MCF catalyst at 430 °C.

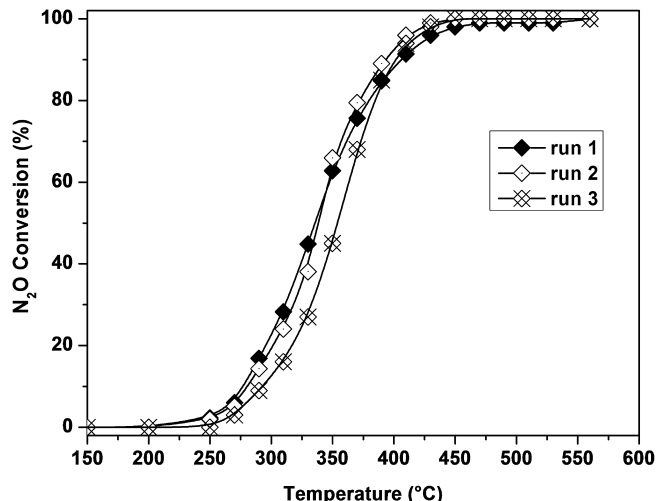


**Fig. 15.** Stability study of the Rh-MCF catalyst for three successive catalytic cycles.

rates. In general, the faster the rate of restructuring, the higher the reaction rate, although it has also been observed that rapid restructuring of solid surfaces may cause instability [69].

Hence, experiments have been conducted with a continuous supply of N<sub>2</sub>O to the Rh-MCF catalyst for a time-on-stream of 6 h at a constant temperature (namely at 430 °C) (Fig. 14). As a result, the catalyst showed excellent stability over the time span and no deactivation of the activity occurred during the reaction.

Fig. 15 shows the catalytic performance of the same catalyst, as a function of temperature, for each heating run and kept at 590 °C for 2 h. Similar catalytic results have been achieved during three different cycles and no significant deactivation has been observed in terms of N<sub>2</sub>O conversion.

These findings confirm the good catalytic stability of the RhO<sub>x</sub> particles on the MCF-type support even in severe conditions (namely at 590 °C) and render Rh-MCF materials suitable for further research and future applications.

#### 4. Conclusions

A set of Rh-containing catalysts has been prepared by wet impregnation of mesoporous silicas with different textural properties, and tested for high concentration N<sub>2</sub>O abatement. As a whole,

the best performances, in terms of N<sub>2</sub>O decomposition, have been achieved for the Rh-MCF catalyst, due to the better textural properties of the MCF silica.

In fact, the MCF-type support has a 3-D mesoporosity with ultra-large cells (up to 40 nm), which allow a uniform distribution of small RhO<sub>x</sub> particles ( $\approx 1$  nm) over the high (internal) surface area. Furthermore, the Rh active sites are also readily accessible to N<sub>2</sub>O molecules.

The catalytic activity of the Rh-KIT-6 sample was lower than that of Rh-MCF, but higher than those of Rh-SBA-15 and Rh-MCM-41, showing the key role of 3-D mesoporosity in favouring the dispersion of Rh active sites.

The most promising catalyst (Rh-MCF) has shown the highest amount of Rh<sup>1+</sup> species (acting as Lewis acidic sites), the easiest rhodium reducibility and the greatest abundance of Rh surface sites, a result that has been confirmed by XPS and H<sub>2</sub>-TPR analysis. These physico-chemical properties reflect the different Rh particle sizes and play an important role in the performances of the catalysts.

Finally, a remarkable relationship between the catalytic activity and the dimension of the particles has been observed in the 1–2.5 nm size range, thus confirming the dispersion-sensitivity of N<sub>2</sub>O decomposition over RhO<sub>x</sub> nanoparticles.

## Acknowledgment

The Ministero dell'Università e della Ricerca (MIUR) is acknowledged for sponsoring this research activity (FIRB – Futuro in Ricerca 2012).

## References

- [1] R.E. Dickinson, R.J. Cicerone, *Nature* 319 (1986) 109–115.
- [2] W.B. Tolman, *Angew. Chem. Int. Ed.* 49 (2010) 1018–1024.
- [3] J. Perez-Ramirez, F. Kapteijn, K. Schoffel, J.A. Moulijn, *Appl. Catal. B: Environ.* 44 (2003) 117–151.
- [4] M. Hussain, D. Fino, N. Russo, *J. Hazard. Mater.* 211/212 (2012) 255–265.
- [5] S. Alini, F. Basile, S. Blasioli, C. Rinaldi, A. Vaccari, *Appl. Catal. B: Environ.* 70 (2007) 323–329.
- [6] F. Kapteijn, J. Rodriguez-Mirasol, J.A. Moulijn, *Appl. Catal. B: Environ.* 9 (1996) 25–64.
- [7] Y. Li, J.N. Armor, *Appl. Catal. B: Environ.* 1 (1992) 31–40.
- [8] R.S. Drago, K. Jurczyk, N. Kob, *Appl. Catal. B: Environ.* 13 (1997) 69–79.
- [9] K.S. Chang, H.J. Lee, Y.S. Park, J.W. Woo, *Appl. Catal. A: Gen.* 309 (2006) 129–138.
- [10] E.V. Kondratenko, R. Kraehnert, J. Radnik, M. Baerns, J. Perez-Ramirez, *Appl. Catal. A: Gen.* 298 (2006) 73–79.
- [11] A. Taguchi, F. Schüth, *Microporous Mesoporous Mater.* 77 (2005) 1–45.
- [12] M. Hussain, S.K. Song, J.H. Lee, S.K. Ihm, *Ind. Eng. Chem. Res.* 45 (2006) 536–543.
- [13] M. Hussain, S.K. Song, S.K. Ihm, *Fuel* 106 (2013) 787–792.
- [14] M. Hussain, N. Abbas, D. Fino, N. Russo, *Chem. Eng. J.* 188 (2012) 222–232.
- [15] I. Fechete, Y. Wang, J.C. Védrine, *Catal. Today* 189 (2012) 2–27.
- [16] E. Vunain, R. Malgas-Enus, K. Jalama, R. Meijboom, *J. Sol-Gel Sci. Technol.* 68 (2013) 270–277.
- [17] X. Xu, H. Xu, F. Kapteijn, J.A. Moulijn, *Appl. Catal. B: Environ.* 53 (2004) 265–274.
- [18] M. Hussain, P. Akhter, D. Fino, N. Russo, *J. Environ. Chem. Eng.* 1 (2013) 164–174.
- [19] M. Hussain, D. Fino, N. Russo, *Chem. Eng. J.* 238 (2014) 198–205.
- [20] O.D. Velev, T.A. Jede, R.F. Lobo, A.M. Lenhoff, *Nature* 389 (1997) 447–448.
- [21] Y.M. Liu, W.L. Feng, T.C. Li, H.Y. He, W.L. Dai, W. Huang, Y. Cao, K.N. Fan, *J. Catal.* 239 (2006) 125–136.
- [22] M. Piumetti, B. Bonelli, P. Massiani, Y. Millot, S. Dzwigaj, L. Gaberova, M. Armandi, E. Garrone, *Microporous Mesoporous Mater.* 142 (2011) 45–54.
- [23] M. Piumetti, B. Bonelli, P. Massiani, S. Dzwigaj, I. Rossetti, S. Casale, M. Armandi, C. Thomas, E. Garrone, *Catal. Today* 179 (2012) 140–148.
- [24] J.G. Park, C.H. Ko, K.B. Yi, J.-H. Park, S.-S. Han, S.-H. Cho, J.-N. Kim, *Appl. Catal. B: Environ.* 81 (2008) 244–250.
- [25] K. Soni, B.S. Rana, A.K. Sinha, A. Bhaumik, M. Nandi, M. Kumar, G.M. Dhar, *Appl. Catal. B: Environ.* 90 (2009) 55–63.
- [26] W.J. Lukens, P. Schmidt-Winkel, D. Zhao, J. Feng, G.D. Stucky, *Langmuir* 15 (1999) 5403–5409.
- [27] P. Schmidt-Winkel, W.W. Lukens, D. Zhao, P. Yang, B.F. Chmelka, G.D. Stucky, *J. Am. Chem. Soc.* 121 (1999) 254–255.
- [28] C.-Y. Chen, H.-X. Li, M.E. Davis, *Microporous Mater.* 2 (1993) 17–26.
- [29] M. Kruk, M. Jaroniec, C.H. Ko, R. Ryoo, *Chem. Mater.* 12 (2000) 1961–1968.
- [30] U. Ciesla, F. Schüth, *Microporous Mesoporous Mater.* 27 (1999) 131–149.
- [31] T. Tsioncheva, L. Ivanova, J. Rosenholm, M. Linden, *Appl. Catal. B: Environ.* 89 (2009) 365–374.
- [32] S. Brunauer, L.S. Deming, W.E. Deming, E. Teller, *J. Am. Chem. Soc.* 62 (1940) 1723–1732.
- [33] A. Sayari, Y. Yan, M. Kruk, M. Jaroniec, *J. Phys. Chem. B* 103 (1999) 3651–3658.
- [34] M. Piumetti, B. Bonelli, M. Armandi, L. Gaberova, S. Casale, P. Massiani, E. Garrone, *Microporous Mesoporous Mater.* 133 (2010) 36–44.
- [35] D.Y. Zhao, J.L. Feng, Q.S. Huo, N. Melosh, G.H. Fredrickson, B.F. Chmelka, G.D. Stucky, *Science* 279 (1998) 548–552.
- [36] A. Corma, *Chem. Rev.* 97 (1997) 2373–2419.
- [37] H. Tüysüz, C.W. Lehmann, H. Bongard, B. Tesche, R. Schmidt, F. Schüth, *J. Am. Chem. Soc.* 130 (2008) 11510–11517.
- [38] P. Schmidt-Winkel, W.W. Lukens Jr., P. Yang, D.I. Margolese, J.S. Lettow, J.Y. Ying, G.D. Stucky, *Chem. Mater.* 12 (2000) 686–696.
- [39] K. Polychronopoulou, J.L.G. Fierro, A.M. Efstratiou, *J. Catal.* 228 (2004) 417–432.
- [40] A. Bueno-López, I. Such-Basanez, C. Salinas-Martínez de Lecea, *J. Catal.* 244 (2006) 102–112.
- [41] Y. Wang, Z. Song, D. Ma, H. Luo, D. Liang, X. Bao, *J. Mol. Catal. A: Chem.* 149 (1999) 51–61.
- [42] S. Suohonen, R. Polvinen, M. Valden, K. Kallinen, M. Harkonen, *Appl. Surf. Sci.* 200 (2002) 48–54.
- [43] J.F. Munera, S. Irusta, L.M. Cornaglia, E.A. Lombardo, D.V. Cesar, M. Schmal, *J. Catal.* 245 (2007) 25–34.
- [44] Y.V. Larichev, O.V. Netskina, O.V. Komova, V.I. Simagina, *Int. J. Hydrogen Energy* 35 (2010) 6501–6507.
- [45] C.-P. Hwang, C.-T. Yeh, Q. Zhu, *Catal. Today* 51 (1999) 93–101.
- [46] T. Montini, A.M. Condò, N. Hickey, F.C. Lovely, L. De Rogatis, P. Fornasiero, M. Graziani, *Appl. Catal. B: Environ.* 73 (2007) 84–97.
- [47] T. Montini, L. De Rogatis, V. Gombac, P. Fornasiero, M. Graziani, *Appl. Catal. B: Environ.* 71 (2007) 125–134.
- [48] M. Haruta, *CATTECH* 6 (2002) 102–115.
- [49] H.J. Freund, *Chem. Eur. J.* 16 (2010) 9384–9397.
- [50] S. Schauermann, N. Nilius, S. Shaikhutdinov, H.J. Freund, *Acc. Chem. Res.* 46 (2013) 1673–1681.
- [51] M. Piumetti, M. Armandi, E. Garrone, B. Bonelli, *Microporous Mesoporous Mater.* 164 (2012) 111–119.
- [52] C.M. Leewis, W.M.M. Kessels, M.C.M. van de Sanden, J.W. Niemantsverdriet, *Appl. Surf. Sci.* 253 (2006) 572–580.
- [53] K.I. Hadjiivanov, G.N. Vayssilov, *Adv. Catal.* 47 (2002) 307–511.
- [54] C.D. Zeinalipour-Yazdi, A.L. Cooksy, A.M. Efstratiou, *J. Phys. Chem. C* 111 (2007) 13872–13878.
- [55] A. Maroto-Valiente, I. Rodriguez-Ramos, A. Guerrero-Ruiz, *Catal. Today* 93–95 (2004) 567–574.
- [56] O.M. Roscioni, J.M. Dyke, J. Evans, *J. Phys. Chem. C* 117 (2013) 19464–19470.
- [57] E. Finocchio, G. Busca, P. Forzatti, G. Groppi, A. Beretta, *Langmuir* 23 (2007) 10419–10428.
- [58] Y.D. Scherson, S.J. Aboud, J. Wilcox, B.J. Cantwell, *J. Phys. Chem. C* 115 (2011) 11036–11044.
- [59] K. Yuzaki, T. Yarimizu, K. Aoyagi, S. Ito, K. Kunimori, *Catal. Today* 45 (1998) 129–134.
- [60] J.M. Thomas, R. Raja, D.W. Lewis, *Angew. Chem. Int. Ed.* 44 (2005) 6456–6482.
- [61] J.M. Thomas, *Proc. R. Soc. A* 468 (2012) 1884–1903.
- [62] J.C. Védrine, *Appl. Catal. A: Gen.* 474 (2014) 40–50.
- [63] M. Piumetti, N. Lygeros, *Chem. Today* 31 (2013) 48–52.
- [64] M. Piumetti, N. Lygeros, *Hadronic J.* 36 (2013) 177–195.
- [65] M. Boudart, *Adv. Catal. Relat. Subj.* 20 (1969) 153–177.
- [66] G. Somorjai, *Catal. Lett.* 7 (1990) 169–182.
- [67] G.A. Somorjai, J. Carranza, *Ind. Eng. Chem. Fundam.* 25 (1986) 63–69.
- [68] N. Musselwhite, G.A. Somorjai, *Top. Catal.* 56 (2013) 1277–1283.
- [69] G.A. Somorjai, *Langmuir* 7 (1991) 3176–3182.